

Tunable thermal response of ZnO nanowires

A J Kulkarni¹ and M Zhou^{1,2,3}

¹ The George W Woodruff School of Mechanical Engineering, Georgia Institute of Technology, Atlanta, GA 30332-0405, USA

² School of Materials Science and Engineering, Georgia Institute of Technology, Atlanta, GA 30332-0405, USA

E-mail: min.zhou@gatech.edu

Received 28 June 2007, in final form 17 August 2007

Published 4 October 2007

Online at stacks.iop.org/Nano/18/435706

Abstract

ZnO nanowires with the $[01\bar{1}0]$ growth orientation undergo a reversible phase transformation from wurtzite (WZ) to a graphitic phase (HX) under tensile loading, leading to a pseudoelastic behavior with recoverable strains up to 16%. Here, we report that this phase transform causes a novel transition in thermal response. Molecular dynamics simulations with the Green–Kubo approach are carried out to determine the thermal responses of wires in the 18.95–40.81 Å size range. Results obtained show that the thermal conductivity in the unstressed WZ state is 8.3–8.6 W m⁻¹ K⁻¹ for the sizes considered and is an order of magnitude lower than the corresponding bulk value. Under loading, elastic stretching and the formation of interfaces cause the thermal conductivity to first decrease significantly. As the transformation progresses, the conductivity increases rapidly to 10.1–11.1 W m⁻¹ K⁻¹, or 20.5–28.5% higher than that of the initial WZ-structured wires. The enhancement is primarily due to an increase in atomic packing density, lower anharmonic coupling of phonons and higher surface specularities of the HX-structured wires. This phenomenon offers a means for tuning the thermal behavior of ZnO nanowires.

1. Introduction

A generation of semiconducting nanostructures such as nanowires, nanotubes, nanobelts and nanorods has been developed recently. As functional building blocks, these nanocomponents have a wide variety of potential applications as piezoelectric generators, force sensors, resonators, chemical and biomolecular sensors, transparent conductors, catalysts and nanoelectronic and nanophotonic components [1–6]. Challenges exist for the integration of these structures in nanoelectronic systems due to high electric field strength and high heat flux at the nanoscale. In particular, heat dissipation and thermomechanical reliability are of great concern. One issue in this regard is that the thermal conductivities of nanostructures are 1–2 orders of magnitude lower than corresponding bulk values due to boundary scattering of phonons [7–15].

The coupling between the mechanical and thermal responses of these materials provides a mechanism for

tuning and increasing the thermal conductivity through the application of mechanical input. Transitions in thermal conductivity and the coefficient of thermal expansion under pressure have been reported for the quartz–coesite, olivine– γ -spinel, coesite–stishovite, B1–B2 and pyroxene–garnet transformations in minerals [16–19]. It has also been shown that the thermoelectric properties of bulk antimony bismuth telluride can be tuned and optimized through applied pressure [20]. Although thermal transport at the macro- and nanoscales is well characterized, the effect of stress on the thermal response of nanostructures has not been extensively studied. The analysis of Picu *et al* [21] on the dependence of thermal conductivity of argon on hydrostatic stress provides some insight, without accounting for the effects of phase transformation and surfaces which play a dominant role at the nanoscale since thermal processes are dominated by surface scattering of phonons.

Recently, we reported a novel reversible phase transformation from wurtzite (WZ, $P6_3mc$) to a previously unknown

³ Author to whom any correspondence should be addressed.

graphitic polymorph (HX, $P6_3/mmc$) in $[01\bar{1}0]$ -oriented ZnO nanowires under tensile loading [22, 23]. This discovery has subsequently been confirmed in $[0001]$ -oriented nanoplates with thicknesses below 20 Å (cf [24]) and in nanowires with diameters below 13 Å [25]. Here, we analyze the effect of this transformation on the thermal conductivity of such nanowires. The analysis focuses on variations in thermal conductivity during the elastic stretching of the initial WZ-structured wire, the phase transformation into the HX structure, and upon completion of the phase transformation. The characterization of the thermal response as a function of strain here is important since axial elongation is one of the most relevant modes of deformation for slender 1D nanomaterials.

2. Computational framework

Molecular dynamics (MD) simulations using the Buckingham potential with charge interactions [26, 27] are carried out. The Buckingham potential for ZnO has been shown to accurately predict the equilibrium lattice energy, cell parameters, elastic and dielectric constants. Extensive perfect lattice, defect and monovalent ion incorporation simulations have been successfully carried out using this potential [26, 28, 29]. The potential also effectively predicts surface properties such as surface energies [29]. This aspect is especially important in the simulations for nanowires whose high surface-to-volume ratios are known to significantly affect behavior. Recently, MD simulations on nanowires using this potential yielded thermal and mechanical behaviors that are in excellent agreement with the predictions of first-principles calculations [14, 23].

The nanowires considered are single-crystalline and wurtzite-structured, with lattice constants $a = 3.249$ Å and $c = 5.206$ Å and a growth direction along the $[01\bar{1}0]$ axis [4, 5]. Three different cross-sectional sizes (21.22×18.95 , 31.02×29.42 and 40.81×39.89 Å²) are considered. The smallest cross-sectional size (21.22 Å \times 18.95 Å) is chosen such that the short-range cutoff distance in the Buckingham potential [26, 27] is smaller than the smallest wire dimension and long-range interactions are properly considered [30]. Periodic boundary conditions are specified in the axial direction. Calculations with different computational cell sizes show that any length greater than 100 Å, irrespective of the cross-section size, is sufficient to avoid image effects [14, 15]. Here, a periodic computational cell length of 150.83 Å is used for all the cross sections analyzed.

The deformation of the nanowires is approximated as a quasi-static process with each deformation increment achieved through successive loading and equilibration steps using a combination of algorithms for NPT and NVE ensembles [31]. Specifically in each deformation increment, stretching at a specified rate of 0.005 ps⁻¹ is first carried out for 0.5 ps using a modified version of the NPT algorithm of Melchionna *et al* [32, 33]. Subsequently, with the strain maintained constant, the nanowire is relaxed for 3 ps via an algorithm for NVE ensemble [31] at the specified temperature. This equilibration duration is chosen such that a statistically steady state is reached and no further structural changes occur.

Since the loading proceeds in a series of equilibration steps, an equilibrium approach such as the Green–Kubo method can be used to determine the thermal response of

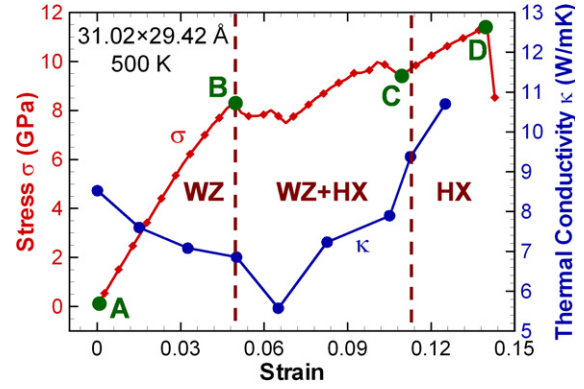


Figure 1. Stress and thermal conductivity as functions of applied strain for a 31.02 Å \times 29.42 Å under tensile loading at 500 K. (This figure is in colour only in the electronic version)

the nanowires as a function of strain. Also, since the MD calculations for determining heat flux do not require any *a priori* knowledge of the heat transport processes or material configuration, this approach is ideal for evaluating heat transfer in materials undergoing deformation or phase transformation. At each strain, the thermal conductivity can be calculated according to the fluctuation–dissipation theorem as

$$\kappa_{\mu\nu} = \frac{1}{Vk_B T^2} \int_0^\infty \langle J_\mu(t) J_\nu(0) \rangle dt, \quad (1)$$

where V is system volume, T is temperature, k_B is the Boltzmann constant, $J_\mu(t)$ is the μ th ($\mu, \nu = 1, 2, 3$) component of the heat current and $\langle J_\mu(t) J_\nu(0) \rangle$ is the autocorrelation function for $J_\mu(t)$ with $\langle \rangle$ denoting ensemble time average. The analysis is conducted at 500 K which is above the Debye temperature θ_D ($=420$ K for ZnO). Consequently, temperature can be calculated from

$$\frac{3}{2} N k_B T = \frac{1}{2} \sum_{i=1}^N m_i v_i^2, \quad (2)$$

with N being the number of atoms in the system and m_i and v_i being, respectively, the mass and velocity of atom i . Temperatures below θ_D , for which quantum mechanical corrections may be needed, are not considered here.

3. Results and discussion

3.1. Variation of thermal conductivity with applied loading

Figure 1 shows stress and thermal conductivity as functions of strain for a 31.02 Å \times 29.42 Å wire. Three distinct stages of deformation can be identified from the stress–strain response: (1) elastic stretching of the defect-free WZ-structured wire (A–B), (2) transformation from WZ to HX (B–C) and (3) elastic stretching of the defect-free HX-structured wire (C–D) after completion of the transformation [22, 23].

3.1.1. WZ-structured wire prior to initiation of phase transformation. The thermal conductivity (κ) of an unstressed 31.02 Å \times 29.42 Å nanowire at 500 K is 8.52 W m⁻¹ K⁻¹, an order of magnitude lower than that for bulk ZnO

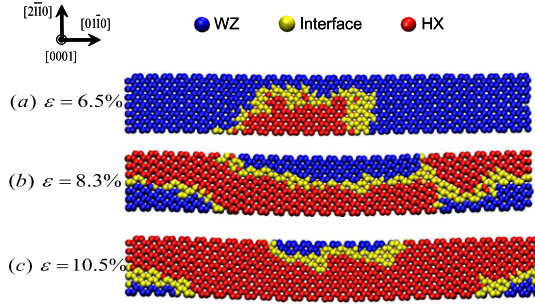


Figure 2. WZ, HX and interface regions in a $31.02 \text{ \AA} \times 29.42 \text{ \AA}$ wire at (a) $\varepsilon = 6.5\%$, (b) $\varepsilon = 8.3\%$ and (c) $\varepsilon = 10.5\%$.

($\sim 100 \text{ W m}^{-1} \text{ K}^{-1}$) [34]. This significant difference is associated with significant boundary scattering of phonons due to the high surface-to-volume ratios of the nanowires and changes in phonon spectrum for the quasi-1D wire structures. Specifically, the relatively large fractions of surface atoms enhance surface scattering of phonons and decrease the phonon mean free path, resulting in lower conductivity which is proportional to the mean free path. In contrast, the characteristic length for bulk materials is much longer and the effect of boundary scattering is negligible, resulting in longer mean free paths and much higher conductivity values [14, 15]. Furthermore, changes in the phonon spectrum at the nanoscale modify phonon group velocities and scattering mechanisms and can also lead to lower thermal conductivity values and size effects [7, 35–37].

As deformation progresses, κ decreases from its initial value of $8.52 \text{ W m}^{-1} \text{ K}^{-1}$ by 19.6% as the strain increases to 0.049. During this stage, the nanowire is fully within the WZ structure and the decrease in κ is primarily due to the nonlinear elastic behavior of WZ along the $[01\bar{1}0]$ orientation, although the increase in lattice anharmonicity at finite values of strain also has a contribution [21]. The nonlinear elastic response can be quantified through the rate of change of the uniaxial modulus

$$E' = \frac{d^2\sigma}{d\varepsilon^2} = \frac{1}{V} \frac{d^3U}{d\varepsilon^3}, \quad (3)$$

where V is the initial volume of the wire, U is the strain energy, and σ and ε are, respectively, the stress and strain along the wire. For the $[01\bar{1}0]$ nanowire analyzed, $E' = -1428.7 \text{ GPa}$ and the modulus E decreases by 35% up to the strain at transformation initiation ($\varepsilon = 0.049$). The elastic stretching also causes the volume of the wire to increase and the mass density ρ to decrease. Both changes combine to cause the stress wave speed or the phonon group velocity \bar{v} ($=\sqrt{E/\rho}$) to decrease by 18.9%. Additionally, the decrease in density along with the lattice distortion increases lattice anharmonicity and, consequently, causes the mean free path (Λ) of the phonons to decrease. At temperatures above the Debye temperature, the kinetic theory of fluids relates thermal conductivity to phonon mean free path through [38]

$$\kappa = \frac{1}{3} C_v \bar{v} \Lambda, \quad (4)$$

where C_v is specific heat. Obviously, the conductivity decreases as the WZ-structured nanowire is stretched.

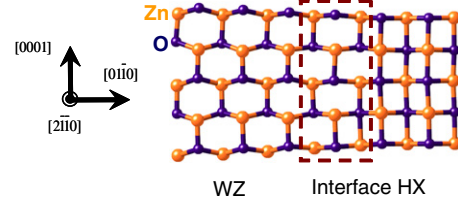


Figure 3. Arrangement of atoms on a $(2\bar{1}10)$ plane across an interfacial region.

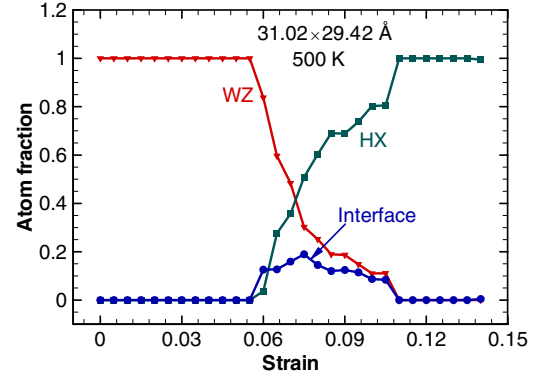


Figure 4. Fractions of atoms in WZ, HX and interface regions as functions of strain for a $31.02 \text{ \AA} \times 29.42 \text{ \AA}$ wire.

3.1.2. WZ/HX-structured wire during phase transformation.

Upon the initiation of phase transformation at $\varepsilon = 0.049$, the stress drops precipitously, reflecting a relaxation of the wire structure. Figure 2 shows the configurations of the wire at $\varepsilon = 0.065, 0.083$ and 0.105 . Three zones, corresponding to WZ, HX and a transitional interface between the two phases, are seen. The nucleation of HX is at the surfaces. The atomic structure on the $(2\bar{1}10)$ plane in the interfacial region is shown in figure 3. Obviously, the interface is coherent and the orientation relationships are maintained in both phases across the interface. The fractions of atoms in the HX, WZ and interfacial regions are shown in figure 4 as functions of strain. Initially ($0.049 < \varepsilon < 0.072$, strain range from transformation initiation to the formation of the largest interface fraction), the fraction of the HX phase is lower than that of the WZ phase and the thermal response is dominated by the conductivity of the WZ phase and the thermal resistance of the interface. In this stage, κ decreases by 18.7% from 6.86 to $5.58 \text{ W m}^{-1} \text{ K}^{-1}$ as the strain increases from 0.049 to 0.072 . This decrease is due to the low thermal transmission coefficient of the interface and enhanced phonon scattering due to (1) discontinuities in the lattice across the interface and (2) lattice distortion associated with the elastic strain field near the interface [39, 40]. Note that over this strain interval the fraction of interfacial atoms increases from 0.12 to a maximum of 0.19 . Since the interfacial thermal resistance is proportional to the area of interfaces (quantified here through the fraction of interfacial atoms), κ decreases as strain increases. Continuation of loading beyond $\varepsilon = 0.072$ causes the fraction of HX to exceed that of WZ (figures 2(b), (c) and 4), resulting in the overall thermal response of the wire to be dominated by the HX phase. At the completion of the WZ \rightarrow HX transformation ($\varepsilon = 0.113$),

the conductivity of the HX-structured wire is $9.4 \text{ W m}^{-1} \text{ K}^{-1}$ or 68.3% higher than the lowest value of $5.58 \text{ W m}^{-1} \text{ K}^{-1}$ at $\varepsilon = 0.072$. This increase in κ is due to several factors, including (1) the higher thermal conductivity of the HX phase (details later), (2) significant decrease (43.3%) in the fraction of interface atoms as the strain increases from 0.072 to 0.113 and (3) the alignment of the interfaces along the direction of heat flow (wire axis) as deformation progresses (figures 2(b) and (c)). Arising primarily from bonding state non-uniformity and lattice strains, interfacial thermal resistance is expected to be much lower for directions parallel to an interface than that for the direction perpendicular to it.

3.1.3. HX-structured wire after transformation. The WZ \rightarrow HX transformation completes at a strain of $\varepsilon = 0.113$. At this stage, some point defects exist due to local variations in the lattices. Further loading causes the defects to disappear, leading to a defect-free HX structure at $\varepsilon = 0.125$. The value of thermal conductivity obtained for this defect-free structure is reported as the characteristic thermal property of the HX wires. Further loading causes the conductivity to decrease, reflecting the nonlinear elastic behavior of the HX-structured wires (not shown). The thermal conductivity of the HX-structured wire in this state is $10.7 \text{ W m}^{-1} \text{ K}^{-1}$, which is 25.6% higher than that of the unstressed WZ wire. Such a significant increase in κ can be qualitatively explained using a simplified model for thermal conductivity [18, 41]. At temperatures above the Debye temperature, the lattice thermal conductivity is limited by anharmonic coupling of phonons and can be expressed as (cf [18, 41])

$$\kappa \approx A \frac{r \bar{v}^3}{3\gamma^2 T} \rho, \quad (5)$$

where r is the average interatomic spacing such that the unit cell volume $V_{\text{cell}} = r^3$, \bar{v} is the average wave speed, ρ is mass density, γ is the thermal Gruneisen parameter, T is temperature and A is a constant representing the contributions of changes in crystal structure (coordination, bond length, etc.) to thermal conductivity. During the WZ \rightarrow HX transformation, the number of atoms per unit cell remains the same and the average bond length increases only by $\sim 6\%$. Hence, the change in A is negligible and, at a given temperature, the effect of the phase transformation on thermal conductivity can be expressed through the change in density, anharmonicity of the lattice and the wave speed as

$$\frac{\kappa_{\text{HX}} - \kappa_{\text{WZ}}}{\kappa_{\text{WZ}}} \approx \left(\frac{\bar{v}_{\text{HX}}}{\bar{v}_{\text{WZ}}} \right)^3 \left(\frac{\rho_{\text{HX}}}{\rho_{\text{WZ}}} \right) \left(\frac{\gamma_{\text{WZ}}}{\gamma_{\text{HX}}} \right)^2 - 1. \quad (6)$$

The wave speed \bar{v} , calculated from the elastic moduli and densities of each of the two phases, is lower for HX than for WZ. Therefore, the change in wave speed tends to lower thermal conductivity and this effect is only secondary. Dominant effects that cause the thermal conductivity to increase come from the higher density and higher Gruneisen parameter of HX. During the transformation, the lattice parameter along the [0001] direction (c) decreases considerably, causing the cell volume to decrease by 11.98% and the density of the structure to increase by 13.5%. The efficient packing of the HX structure and its higher density lead to a lower anharmonicity (lower thermal Gruneisen parameter)

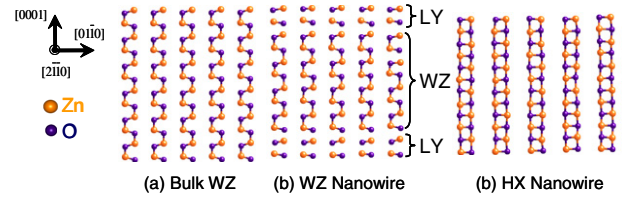


Figure 5. Arrangement of atoms in the interior and on the surfaces of a $31.02 \text{ \AA} \times 29.42 \text{ \AA}$ wire, the images correspond to (a) bulk WZ, (b) WZ-structured wire with LY-structured surfaces after initial relaxation and (c) HX-structured wire after completion of the WZ \rightarrow HX transformation.

and, ultimately, the higher thermal conductivity [17]. For the $31.02 \text{ \AA} \times 29.42 \text{ \AA}$ wire, the 25.6% increase in κ implies a 27.5% decrease in γ relative to the value of 0.69 for WZ at 500 K [42]. This decrease is consistent with the increase in packing efficiency of the HX structure over the parent WZ structure. A quantitative prediction of γ is not feasible here since the model is strictly valid for bulk materials where the effect of surface scattering of phonons is negligible. Nevertheless, this model provides a qualitative explanation for the increase in conductivity observed here.

The difference in surface configurations between WZ- and HX-structured nanowires also contributes to the observed increase in thermal conductivity. To illustrate this issue, figures 5(a) and (b) show the positions of atoms on layers perpendicular to the [0001] direction for bulk WZ and a WZ-structured wire and figure 5(c) shows the configuration of a HX-structured nanowire. For WZ wires, the imbalance of ionic forces on the surfaces due to the reduced number of neighbors and surface polarity cause extensive surface reconstruction relative to bulk WZ. Obviously, this reconstruction entails the contraction of surface layers and merging of Zn and O basal planes (figures 5(a) and (b)), resulting in a layered surface structure (LY) which is crystallographically similar to the HX structure [43, 44]. Such reconstructions modify atomic arrangement on surfaces relative to the core of the nanowire and alter the surface scattering behavior of phonons, causing the surface specularly and, hence, the thermal conductivity for WZ-structured nanowire to be much lower than that for bulk WZ. In the HX-structured wire in figure 5(c), the atomic arrangement on surfaces is similar to that in the core and hence the surface disorder is significantly lower than that of the WZ wire in figure 5(b). As a result, the surface specularly for HX wires is much higher than that of WZ-structured nanowires, resulting in much lower effects of boundary scattering and higher conductivity values. The effect of surface specularly on conductivity can be characterized through equation (4). Under conditions for which phonon-phonon and phonon-defect interactions are negligible, the phonon mean free path can be expressed as [45]

$$\Lambda = \frac{d}{(1-p)}, \quad (7)$$

where p is the probability of specular scattering (a function of surface roughness and temperature) and d is the effective size of the nanowire. For a body with perfectly specular (atomistically smooth) surfaces, $p = 1$. Consequently, the

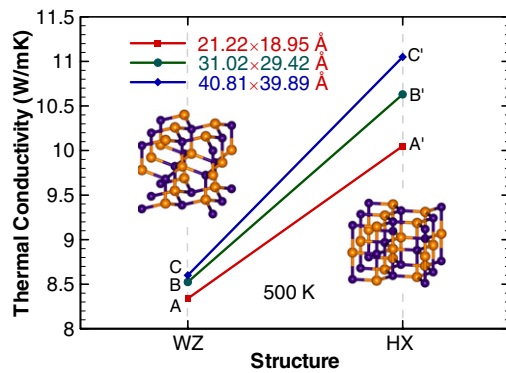


Figure 6. Thermal conductivity of unstressed WZ and transformed HX wires of three different sizes.

phonon mean free path is infinite and the thermal conductivity is not affected by boundary scattering. On the other hand, for a body with perfectly diffuse surfaces, $p = 0$ and the mean free path expression reduces to the Casimir limit such that the mean free path of the phonons is limited by the size of the nanowire. In reality, the specularity value is between the limiting cases ($0 < p < 1$) and depends significantly on surface attributes. As discussed previously, the surface specularity of WZ wires is much lower than that of HX wires. Consequently, for nanowires with the same characteristic sizes, the phonon mean free path and therefore the conductivity of the HX wires is higher than that of the WZ wires.

3.2. Size dependence of thermal conductivity

The bulk and surface effects discussed above combine to give rise to significant dependence of behavior on wire size. Figure 6 shows the conductivity values of unstressed WZ and transformed HX wires of three different sizes. For WZ wires, the thermal conductivity is in the range of 8.3–8.6 $\text{W m}^{-1} \text{K}^{-1}$ which is an order of magnitude lower than that for bulk ZnO and decreases by 3% as the lateral size decreases from 40.81 × 39.89 to 21.22 × 18.95 Å^2 . This trend results directly from the higher surface-to-volume ratios and smaller mean free path at the smaller sizes. A clear dependence of conductivity on size is also seen for the HX-structured wires. The WZ-to-HX transformation causes the conductivity to increase to 10.1, 10.7 and 11.1 $\text{W m}^{-1} \text{K}^{-1}$ for the 21.22 × 18.95, 31.02 × 29.42 and 40.81 × 39.89 Å^2 nanowires, respectively. The 20–28% increase over the values for WZ wires is associated with the lower anharmonicity due to the higher surface specularity of the HX wires.

4. Conclusions

MD simulations with the Green–Kubo approach are carried out to determine the thermomechanical response of [01 $\bar{1}$ 0]-oriented ZnO nanowires under tensile loading. Three distinct stages in the thermal and mechanical responses are observed. The mechanical response consists of (1) elastic stretching of WZ, (2) phase transformation from WZ to HX and (3) elastic stretching of HX. The thermal conductivity of the nanowires is a function of applied strain in each of the three stages.

Over the size range of 18.95–40.81 Å , the elastic stretching in the WZ structure is accompanied by 19–27% decrease in the thermal conductivity. The nonlinearity of the elastic response of the wires with lower stiffness (hence lower wave speeds) at higher strains is the origin of this effect. The formation of interfaces during the WZ-to-HX phase transformation causes the thermal conductivity to decrease by another 15–19% as the transformation progresses. Upon completion of the transformation, the thermal conductivity for the HX-structured wires are 20.5–28.5% higher than those of the corresponding WZ-structured wires. This increase in conductivity is due to the higher atomic packing density, lower anharmonic coupling of phonons and higher surface specularity of the HX wires.

Novel phase transformations at the nanoscale, like the one analyzed here, alter thermal conductivity and provide a mechanism for controlling or ‘tuning’ the thermal response of nanocomponents through the application of a mechanical input. The present analysis considers the thermomechanical response of ZnO since it is a versatile semiconducting material with applications in power generation, sensing, environmental monitoring, biomedical systems and communications technology. It should be noted that such phase transformations can also occur in other group IV, III–V and II–VI materials including InN, GaN and SiC [46], leading to a similar potentially exciting tunability of thermal responses in these materials as well. The thermomechanical coupling in these materials may therefore provide both opportunities for developing ‘tunable’ functional nanodevices and challenges for ensuring thermomechanical reliability and functionality of a range of NEMS.

Acknowledgments

Support through NSF grant no. CMS9984298 and NSFC grant no. 10528205 is gratefully acknowledged. Computations are carried out at the NAVO and ASC MSRCs through AFOSR MURI no. D49620-02-1-0382. AJK thanks Thomas E Beechem III for valuable discussions.

References

- [1] Arnold M S, Avouris P, Pan Z W and Wang Z L 2003 *J. Phys. Chem.* **107** 659
- [2] Gao P X and Wang Z L 2005 *J. Appl. Phys.* **97** 044304
- [3] Wang X, Zhou J, Song J, Liu J, Xu N and Wang Z L 2006 *Nano Lett.* **6** 2768
- [4] Wang Z L 2004 *J. Phys.: Condens. Matter* **16** R829
- [5] Wang Z L 2004 *Annu. Rev. Phys. Chem.* **55** 159
- [6] Wang Z L and Song J 2006 *Science* **312** 242
- [7] Volz S G and Chen G 1999 *Appl. Phys. Lett.* **75** 2056
- [8] Li D, Wu Y, Kim P, Shi L, Yang P and Majumdar A 2003 *Appl. Phys. Lett.* **86** 2934
- [9] Lu X, Shen W Z and Chu J H 2002 *J. Appl. Phys.* **91** 1542
- [10] Shi L, Hao Q, Yu C, Mingo N, Kong X and Wang Z L 2004 *Appl. Phys. Lett.* **84** 2638
- [11] Cahill D G, Ford W K, Goodson K E, Mahan G D, Majumdar A, Maris H J, Merlin R and Phillpot S R 2003 *J. Appl. Phys.* **93** 793
- [12] Lu X, Chu J H and Shen W Z 2003 *J. Appl. Phys.* **93** 1219
- [13] Walkauskas S G, Broido D A, Kempa K and Reinecke T L 1999 *J. Appl. Phys.* **85** 2579
- [14] Kulkarni A J and Zhou M 2006 *Acta Mech. Sin.* **22** 217
- [15] Kulkarni A J and Zhou M 2006 *Appl. Phys. Lett.* **88** 141921
- [16] Andersson P 1985 *J. Phys. C: Solid State Phys.* **18** 3943

- [17] Jeanloz R and Roufosse M 1982 *J. Geophys. Res.* **87** 10763
- [18] Roufosse M C and Jeanloz R 1983 *J. Geophys. Res.* **88** 7399
- [19] Slack G A and Ross R G 1985 *J. Phys. C: Solid State Phys.* **18** 3957
- [20] Polvani D A, Meng J F, Shekar N V C, Sharp J and Badding J V 2001 *Chem. Mater.* **13** 2068
- [21] Picu R C, Borca-Tasiuc T and Pavel M C 2003 *J. Appl. Phys.* **93** 3535
- [22] Kulkarni A J, Sarasamak K, Limpijumnong S and Zhou M 2007 *Phil. Mag.* **87** 2117
- [23] Kulkarni A J, Zhou M, Sarasamak K and Limpijumnong S 2006 *Phys. Rev. Lett.* **97** 105502
- [24] Zhang L and Huang H 2006 *Appl. Phys. Lett.* **89** 183111
- [25] Zhang L and Huang H 2007 *Appl. Phys. Lett.* **90** 023115
- [26] Binks D J and Grimes R W 1993 *J. Am. Ceram. Soc.* **76** 2370
- [27] Wolf D, Koblinski P, Phillpot S R and Eggebrecht J 1999 *J. Chem. Phys.* **110** 8254
- [28] Grimes R W, Binks D J and Lidiard A B 1995 *Phil. Mag. A* **72** 651
- [29] Binks D J 1994 Computational modelling of zinc oxide and related oxide ceramics *PhD Thesis* University of Surrey, Harwell
- [30] Kulkarni A J, Zhou M and Ke F J 2005 *Nanotechnology* **16** 2749
- [31] Haile J M 1997 *Molecular Dynamics Simulation* (New York: Wiley-Interscience)
- [32] Melchionna S, Ciccotti G and Holian B L 1993 *Mol. Phys.* **78** 533
- [33] Spearot D, Jacob K and McDowell D M 2005 *Acta Mater.* **53** 3579
- [34] Wolf M W and Martin J J 1973 *Phys. Status Solidi* **17** 215
- [35] Balandin A and Wang K L 1998 *Phys. Rev. B* **58** 1544
- [36] Balandin A, Nika D L and Pokatilov E P 2004 *Phys. Status Solidi c* **1** 2658
- [37] Zou J and Balandin A 2001 *J. Appl. Phys.* **89** 2932
- [38] Majumdar A 1993 *J. Heat Transfer* **115** 7
- [39] Klemens P G 1954 *Proc. Phys. Soc. LXVIII* **12-A** 1113
- [40] Klemens P G 1994 *Int. J. Thermophys.* **15** 1345
- [41] Roufosse M and Klemens P G 1973 *Phys. Rev. B* **7** 5379
- [42] Gadzhiev G G 2003 *High Temp.* **41** 778
- [43] Claeysens F, Freeman C L, Allan N L, Sun Y, Ashfold M N R and Harding J H 2005 *J. Mater. Chem.* **15** 139
- [44] Freeman C L, Claeysens F, Allan N L and Harding J H 2006 *Phys. Rev. Lett.* **96** 066102
- [45] Zou J and Balandin A 2001 *J. Appl. Phys.* **89** 2932
- [46] Sarasamak K, Kulkarni A J, Zhou M and Limpijumnong S 2007 *Phys. Rev. B* submitted